THE JOURNAL OF BIOLOGICAL CHEMISTRY VOL. 286, NO. 24, pp. 21353–21360, June 17, 2011
© 2011 by The American Society for Biochemistry and Molecular Biology, Inc. Printed in the U.S.A.

Conserved Interaction between Transferrin and Transferrin-binding Proteins from Porcine Pathogens*[S]

Received for publication, January 31, 2011, and in revised form, April 4, 2011 Published, JBC Papers in Press, April 12, 2011, DOI 10.1074/jbc.M111.226449

Leslie P. Silva[‡], Ronghua Yu[§], Charles Calmettes[¶], Xue Yang[§], Trevor F. Moraes[¶], Anthony B. Schryvers[‡§1], and David C. Schriemer[‡2]

From the [‡]Departments of Biochemistry and Molecular Biology and [§]Microbiology, Immunology, and Infectious Diseases, University of Calgary, Calgary, Alberta T2N 1N4, Canada and the [¶]Department of Biochemistry, University of Toronto, Toronto, Ontario M5A 2N4, Canada

Gram-negative porcine pathogens from the Pasteurellaceae family possess a surface receptor complex capable of acquiring iron from porcine transferrin (pTf). This receptor consists of transferrin-binding protein A (TbpA), a transmembrane iron transporter, and TbpB, a surface-exposed lipoprotein. Questions remain as to how the receptor complex engages pTf in such a way that iron is positioned for release, and whether divergent strains present distinct recognition sites on Tf. In this study, the TbpB-pTf interface was mapped using a combination of mass shift analysis and molecular docking simulations, localizing binding uniquely to the pTf C lobe for multiple divergent strains of *Actinobacillus plueropneumoniae* and *suis*. The interface was further characterized and validated with site-directed mutagenesis. Although targeting a common lobe, variants differ in preference for the two sublobes comprising the iron coordination site. Sublobes C1 and C2 participate in high affinity binding, but sublobe C1 contributes in a minor fashion to the overall affinity. Further, the TbpB-pTf complex does not release iron independent of other mediators, based on competitive iron binding studies. Together, our findings support a model whereby TbpB efficiently captures and presents iron-loaded pTf to other elements of the uptake pathway, even under low iron conditions.

Bacteria are dependent upon effective and efficient iron acquisition mechanisms to survive and proliferate in the iron-limited environment of the host (1–3). Pathogenic Gram-negative bacteria within the Neisseriaceae and Pasteurellaceae families rely on specialized uptake systems to acquire iron directly from host iron-binding proteins (2–5). These bacteria can acquire iron from host transferrin (Tf)[3] in particular (6), but in some cases also lactoferrin (7, 8) and hemogobulin/haptoglobulin (9). To understand such uptake mechanisms, a detailed characterization of relevant receptor-host protein interactions is required.

The bacterial Tf receptors are composed of two iron-repressible surface components, transferrin binding protein A (TbpA), a TonB-dependent integral outer membrane protein of ~100 kDa, and transferrin-binding protein B (TbpB), a lipoprotein varying in size from 60 to 100 kDa (2, 3, 5, 10, 11). They have been found in clinical isolates of the Neisseriaceae, Pasteurellaceae, as well as the Moraxellaceae families (12) and constitute the outer membrane receptor complex responsible for binding Tf and transporting iron across the outer membrane into the periplasmic space (4, 13). These receptors exhibit a strict host specificity. For example, receptors of porcine pathogens will specifically bind porcine transferrin (pTf) but not human, avian, bovine, or ovine Tf (14).

Tf is a glycoprotein of ~80 kDa, composed of two highly homologous N and C lobes (15). Each lobe contains two domains, connected by two antiparallel β-strands in a clam-shell-like fold, producing a cleft that coordinates Fe^{3+} in the binding pocket, along with a synergistic anion (CO_3^{2-} or $C_2O_4^{2-}$) (16–18). Crystal structures of several full-length Tfs from different species reveal a significant conformational change upon iron binding, resulting in a closing of the cleft around the coordinated iron (19). Apo- and holo-Tf forms have different affinities for the bacterial Tbp receptors. Unlike TbpA, the TbpBs have a strong preference for binding to the holo-form of Tf (20–23), which suggests that TbpB may play a role in efficient capture of the holo-form of Tf (24, 25). For the *Actinobacillus* spp., *in vitro* studies have shown that a TbpB-deficient strain could utilize Tf-bound iron, but was avirulent (26). This potential for diverse receptor-Tf recognition mechanisms provides a rationale for characterizing Tf-TbpB interactions across multiple variants. The sequence heterogeneity for TbpB proteins in particular is considerable, with 47–82% sequence identity observed in variants from a cross-section of pathogenic strains (25, 27). Therefore, this study seeks to determine the impact of such heterogeneity on the interaction with Tf, from the perspective of Tf.

A survey of existing binding studies suggests that TbpB interacts with Tf through the receptor N lobe (28) and the Tf C lobe (11, 22, 29, 30). Recent work by Ling *et al.* has described two TbpB variants from *Neisseria meningitidis* that interact with the C lobe of human transferrin (hTf) (11), although it has been previously reported that both Tf lobes are involved in binding,

* This work was supported by the Canadian Foundation for Innovation, the Canada Research Chair program, the Alberta Heritage Foundation for Medical Research, and the Canadian Institutes of Health Research.

[S] The on-line version of this article (available at http://www.jbc.org) contains supplemental Figs. 1–8 and additional references.

[1] To whom correspondence may be addressed. E-mail: schryver@ucalgary.ca.

[2] To whom correspondence may be addressed. E-mail: dschriem@ucalgary.ca.

[3] The abbreviations used are: Tf, transferrin; *Ap*, *Actinobacillus pleuropneumoniae*; *As*, *Actinobacillus suis*; FbpA, ferric-binding protein A; H/DX, hydrogen/deuterium exchange; hTf, human transferrin; Mbp, maltose-binding protein; MS/MS, tandem mass spectrometry; pTf, porcine transferrin; SUPREX, stability of unpurified proteins from rates of H/D exchange; TbpA, Tf-binding protein A; TbpB, Tf-binding protein B; TCEP, Tris(2-carboxyethyl) phosphine.

Downloaded from http://www.jbc.org/ at UNIVERSITY OF CALGARY on August 17, 2017

specifically for *Moraxella catarrhalis* (23) and the ovine pathogen *Haemophilus paragallinarum* (30). By taking advantage of structural information available for divergent TbpBs from porcine pathogens (5, 31), the current study was initiated to determine how the considerable variability in the TbpB surface regions maintain the interaction with pTf. Together with a companion study by Calmettes *et al.* (31), we provide a structural analysis of the receptor-Tf interaction representing several divergent porcine pathogenic strains and evaluate the impact of iron loading on the molecular recognition mechanism in greater detail.

Recently available protein structures provide an opportunity to map interactions with pTf at high resolution, using a hybridized strategy based on mass shift mapping that involves hydrogen/deuterium exchange (H/DX) methods and structural modeling (32, 33). Shift mapping was recently applied to hTf (11); however, the absence of a reliable human pathogenic TbpB structure prevented a detailed characterization of the transferrin binding site. In the current study, shift mapping was used to locate interfaces and altered dynamics upon the binding of pTf to four TbpB variants. These mapping data were used to test heterodimer models arising from computational docking of pTf to available TbpB structures (5, 31). The models were further tested through mutations and surface plasmon resonance binding studies, as guided by hot spot analysis. Our findings reveal that all four receptor variants interact at a partially conserved interface on the C lobe of Tf and highlight how iron loading renders the C lobe uniquely capable of binding to TpbB.

EXPERIMENTAL PROCEDURES

Production of Recombinant TbpB—The mature coding region of TbpB from *Actinobacillus pleuropneumoniae* strain *Ap*H49 (serotype7), *Ap*H87 (serotype 5), *Ap*H89 (serotype 1) and *Actinobacillus suis As*H57 were PCR-amplified and cloned in to the in-frame BamHI restriction site of a customized expression vector preceded by a polyhistidine region, a maltose-binding protein (Mbp) and a tobacco etch virus protease cleavage site. *E. coli* strain C43 cells transformed with the recombinant plasmids were grown in 1 liter of Luria base (LB) broth supplemented with ampicillin (100 μl/ml) for 20 h at 37 °C. Cells were harvested by centrifugation at 7,000 $\times$ *g* for 10 min, resuspended in 30 ml of resuspension buffer (50 mM NaCl, 50 mM Tris, pH 8.0), and lysed with a Emulsiflex cell homogenizer (Avestin Inc., Ottawa, ON, Canada). The cell lysate was centrifuged at 40,000 $\times$ *g* for 20 min, and the supernatant was applied to a Ni^{2+}-nitrilotriacetic acid column to isolate the Mbp-TbpB fusion protein. After elution from the column and dialysis in buffer, the Mbp tag was cleaved from the TbpBs by tobacco etch virus protease digestion overnight, at room temperature. The digestion mixture was applied to a Ni^{2+}-nitrilotriacetic acid column to remove the Mbp and His-tagged recombinant tobacco etch virus. The purified TbpBs were dialyzed against 50 mM NaH_2PO_4, 0.3 M NaCl, 5 mM imidazole, pH 8.0.

Production and Purification of pTf—Recombinant pTfs were produced from a *Pichia pastoris* expression system, followed by iron loading. Briefly, recombinant pTf expressed from a modified pPICαA vector (Invitrogen) in *P. pastoris* was precipitated from the culture supernatant by ammonium sulfate. After centrifugation, the pellet was then resuspended in water, and the solution was dialyzed against 10 mM HEPES, pH 7.0, overnight at 4 °C. The dialyzed solution was applied to a Q-Sepharose column and eluted via an NaCl gradient. The purified solution was dialyzed against 10 mM HEPES, pH 7.0, and then analyzed by SDS-PAGE.

Site-directed mutagenesis of pTf to generate R509A, D360A, and S625K mutations was performed using the Invitrogen Geneart® Site-directed Mutagenesis System, as initially described by Weiner *et al.* (34). Expression of the mutants followed the same procedure as wild type.

FbpA Protein production—Wild-type *Haemophilus influenzae* FbpA was expressed and iron loaded as described by Shouldice *et al.* (35). To generate apo-FbpA, holo-FbpA was extensively dialyzed against 100 mM sodium acetate, 100 mM sodium phosphate monobasic, 10 mM EDTA, pH 5.5, at 4 °C overnight, to release the iron. The sample was then dialyzed extensively against 10 mM HEPES, pH 7.0, at 4 °C. SDS-PAGE was used to confirm the purity of the protein preparation.

TbpB-pTf Complex Formation—A 1.5:1 ratio of purified TbpB was added to holo-pTf in 10 mM HEPES, pH 7.0, buffer and incubated for 1 h at room temperature. After incubation, the samples were applied to a Q-Sepharose anion exchange column. Only the TbpB-Tf complex bound to the column and was eluted by the addition of 200 mM NaCl in the buffer. The pooled fractions were dialyzed extensively against 10 mM HEPES, pH 7.0, at 4 °C.

Mass Shift Analysis by H/DX—Each H/DX experiment involved a measurement of deuteration levels for pTf in the presence and absence of each of the four TbpB receptors. In this fashion, changes in deuteration arising from complexation could be used to identify the binding interface. These measurements were made using mass spectrometry of pTf peptides, generated by digesting deuterated protein under conditions preventing back-exchange of deuterium. Thus, these experiments provided a "peptide-level" resolution of binding interfaces and changes in protein dynamics resulting from binding.

Quadruplicate experiments were performed for each state (free or receptor-bound pTf). In each experiment, protein stock solution was labeled at pH 7.0 in D_2O (25% v/v) at 20 °C for 2 min. The solution was then quenched and reduced on ice for 1.5 min (in 250 mM TCEP, 0.08% TFA (v/v), pH 2.3).

This quenched and reduced protein solution was digested with immobilized pepsin (Applied Biosystems) in a cartridge format (5 cm x 200 μm inner diameter, assembled in-house). The digest was captured on a small C18 reversed-phase column and separated using a 5–90% steep linear gradient of acidified acetonitrile (0.03% trifluoroacetic acid (TFA), 0.02% FA, both v/v), Effluent was directly infused into a QSTAR Pulsar *i* quadrupole time-of-flight (QqTOF) mass spectrometer. Digestion and chromatography were carried out in an ice bath.

To identify the pTf peptides arising from the digests, unlabeled peptides were prepared under similar conditions and sequenced by tandem mass spectrometry (MS/MS). The MS/MS spectra were searched against the pTf sequence with a local installation of Mascot 2.1, using conventional identifica-

Downloaded from http://www.jbc.org/ at UNIVERSITY OF CALGARY on August 17, 2017

tion criteria. 87 peptides were confirmed suitable for subsequent mass shift experiments.

Mass spectral data from each replicate H/DX-MS experiment were analyzed using Hydra v1.5 (36). The criteria used for determining significant mass shifts were described previously by Bennett *et al.* (33). Briefly, significantly shifted peptides must meet the following criteria: a two-tailed *t* test ($p < 0.05$) using pooled standard deviations from quadruplicate analysis of each state and receptor, and exceeding a threshold shift value (±2 S.D.) based on a measurement of the shift noise and assuming a normal distribution. Deuteration data were then color-coded blue and red for positive and negative shifts, respectively, and mapped to pTf structure (Protein Data Bank code 1H76).

Rosetta Docking—The Rosetta models used in this paper were generated as described by Moraes *et al.* (5) and Calmettes *et al.* (31). Briefly, the RosettaDock program was run in full atom mode using standard Monte Carlo movements, allowing for spin around the axis connecting the two proteins. Experimentally determined important residues on the receptor side only were taken into account during docking. Briefly, a program modification checked the RosettaDock-generated decoys for whether the residues designated were within 10 Å of pTf. Decoys that failed on any important residue were deleted. The program was then run continuously until all decoys met each of the designated TbpB distance constraints (31).

KFC Hot Spot Prediction—Rosetta-docked models were submitted to the Mitchell laboratory KFC Hot Spot Prediction server, as described by Darnell *et al.* (37). The software combines two algorithms, K-FADE (Fast Atomic Density Evaluation) which measures shape specificity features, with K-CON, which uses biochemical contact features (37).

Surface Plasmon Resonance—Surface Plasmon resonance experiments were performed using a BiacoreX instrument (GE Healthcare) at 25 °C, similar to those described by Calmettes *et al.* (31). Briefly, four pTf constructs (wild-type and pTf mutants D360A, R509A, and S625K) were coupled to the sensor chip (research-grade CM5) via standard *N*-hydroxysuccinimide and *N*-ethyl-*N*-(dimethylaminopropyl) carbodiimide activation. TbpB orthologs (*Ap*H49, *As*H57, *Ap*H87, and *Ap*H89) were diluted at various concentrations in the mobile phase buffer (10 mM HEPES, pH 7.5, 150 mM NaCl, and 0.005% (v/v) surfactant P20). Samples were injected at a flow rate of 20 μl/min, and bound receptor was subsequently removed by washing with mobile phase for 90 or 240 s after the injection. Regeneration buffer (10 mM HEPES, pH 7.5, 2 M NaCl) was injected prior to each analyte injection. Kinetic constants were calculated from the sensorgrams using the simulated BiacoreX evaluation software, version 4.0.1 (GE Healthcare).

SUPREX Analysis of FbpA—Apo-FbpA was mixed 1:1 with the pTf-TbpB complex and incubated at room temperature with gentle rotation for 1 h. A Microcon filtration device (Millipore) with a molecular weight cutoff of 50,000 g/mol was used to separate FbpA from the complex, followed by concentration with an Amicon 0.5-ml 10,000 g/mol molecular weight cutoff Ultracel 10K membrane centrifugal concentrator (Millipore) (final concentration of 1 mg/ml).

Apo-FbpA, apo-FbpA with complex, and holo-FbpA were treated with increasing concentrations of guanidine hydrochloride (Gdn-HCl), from 0 to 4 M, to generate a SUPREX denaturation curve in a manner similar to the method described by Parker-Siburt *et al.* (13). The mass spectrometer used for detection is the same as described for the HD/X experiments. The Bayesian Protein Reconstruct application from BioAnalyst QS™ version 1.4 (Applied Biosystems) was used to deconvolute the acquired spectra, to generate average centroid masses for each of the labeled FbpA samples. A denaturation curve for each sample was then generated and fit using OriginPro version 8.

Absorption Studies of FbpA—Apo-FbpA was incubated with pTf-TbpB complex as described in the SUPREX experiment. A 50,000 g/mol molecular weight cutoff Microcon filter was used to separate FbpA from the pTf-TbpB complex. FbpA was then analyzed by spectrophotometry at 480 nm. Samples were prepared in triplicate and related to controls (holo-FbpA, apo-FbpA, and pTf-TbpB complex).

As an additional control, apo-FbpA was incubated with $FeCl_3$ in 100 mM sodium bicarbonate, 100 mM sodium citrate, pH 8.6. The remaining free iron was removed via gel filtration chromatography, and the iron-loaded FbpA (apo-FbpA + $FeCl_3$) was concentrated using an Amicon concentrator as described.

RESULTS

Mass Shift Perturbation Mapping of Bound and Free Porcine Tf—The availability of structures for TbpB (5, 31) and pTf (38) makes this an ideal system for investigating the receptor-protein interaction. In this study, mass shift perturbation experiments (33) were carried out using TbpBs from four strains of the porcine pathogens *A. pleuropneumoniae* and *A. suis* to gauge intrapathogen variability with respect to the pTf-TbpB interaction and to extend the previous analyses of human pathogenic receptor interactions (11).

Sequencing of peptides derived from pTf was performed as described by Ling *et al.* (11). A sequence coverage map for pTf can be found in supplemental Fig. 1. To determine whether a shift analysis of peptides from one large protein in the presence of another would be feasible, pTf and TbpB were processed simultaneously, and the ability to detect pTf peptides in this mixture was determined with Hydra v1.5 and manual verification (36). Although the complexity of the spectra increased significantly, there were few instances of peptide overlap and a minimal impact of increased ion suppression on peptide detection. Collectively, the impact on pTf sequence coverage used in our mass shift studies was a reduction from 68% (98 peptides) in the absence of TbpB to 63% (87 peptides) in its presence. Surface and schematic representations demonstrating the degree of sequence coverage are displayed in Fig. 1, mapped onto the holo-pTf structure. Of the 18 disulfide bonds present in pTf (39), 15 peptides representing 8 disulfides were detected. This incomplete coverage is likely due to a combination of incomplete reduction under the conditions required to prevent deuterium back-exchange (most notably temperature and pH) and issues related to peptide detection. To ensure that the disulfide reduction was optimized for this application, extending the reduction time up to 10 min did not significantly increase the

Downloaded from http://www.jbc.org/ at UNIVERSITY OF CALGARY on August 17, 2017

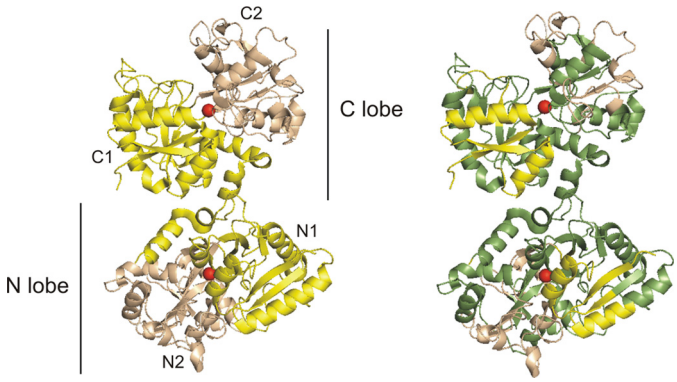

FIGURE 1. **Structural representation of iron-loaded pTf.** The figure highlights the sublobe designations (*left*) and a composite of the sequence coverage available in the mass shift experiments (*right*). Corresponding sublobes are colored *sand* (C2 and N1) and *yellow* (C1 and N2), with Fe^{3+} in *red*. Sequence coverage is shown in *green*. The structure is based on Protein Data Bank entry 1H76.

representation of cysteine-containing peptides (data not shown).

The extent of pTf peptide mass shifts, induced by binding each of the four TbpB variants was determined (Fig. 2). The four receptor variants generated similar patterns of altered deuteration, with peptides showing significant changes relative to free pTf colored in *red*. All significant perturbations map to the C lobe of pTf. None of the four receptor variants caused an increase in solvent accessibility upon pTf binding because there were no significantly increased mass shifts. The significant changes were mapped to the C lobe of pTf for each receptor (Fig. 3). These changes upon complexation can be attributed to newly formed interfacial regions or localized stabilization of structure.

To confirm that these mass shifts were maximized, a saturation analysis was conducted in which shift measurements were monitored as a function of excess receptor. For example, shift values from pTf complexed with *Ap*H87 TbpB in a 1:1 ratio were compared with similar analyses of pTf complexed with 2-fold and 4-fold excesses of the receptor. One-way ANOVA and Tukey tests confirmed that the shift values for each Tf peptide showed no significant change over this range, indicating that pTf was saturated with TbpB at a 1:1 ratio, as expected based upon the receptor purification procedure (see "Experimental Procedures").

This shift saturation provides the opportunity to compare regional differences in shift values across the receptor variants in greater detail (supplemental Fig. 2). The pTf complexes with *Ap*H49 and *Ap*H87 receptor variants display the largest mass shifts in most affected regions of the C lobe and are for the most part equivalent within the error of the measurements. *As*H57 is similar to these two variants, except for a weaker shift in peptides from 629–639. Finally, *Ap*H89 shows the weakest set of shifts among all four receptors in this 629–639 region. Thus, whereas the shift measurements point to a commonly affected region of pTf structure (Fig. 3), there appears to be a moderate degree of variability in the subregions comprising elements of the heterodimer interface.

Correlation of Mass Shift Perturbation Data with Binding Site Prediction—The computational docking of pTf to porcine TbpBs used structures for the *Ap*H49 TbpB variant (5) and the *As*H57 and *Ap*H87 TbpB variants, as described by Calmettes *et al.* (31). There are currently no structures available for *Ap*H89. The top scoring models for the three complexes were used to generate contact surfaces on pTf, representing the three TbpB-pTf interfaces. These contact surfaces highlight all residues on pTf within 5 Å of the corresponding receptor (Fig. 4). These surfaces define an interface spanning both C1 and C2 subdomains of the C lobe that differ little among the variants in total surface area (934 ± 60 $Å^2$).

The computational models in general support the findings of the shift analysis. TbpB docks with the C lobe exclusively, in a manner bridging both C1 and C2 subdomains (interaction models of the remaining complexes can be found in supplemental Fig. 3). Incomplete sequence coverage in the C2 lobe in particular prevents a full shift mapping of the interface, but the data do highlight a region spanning the two subdomains for *Ap*H49 and *Ap*H87, within the peptide resolution of the shift method. The remaining two receptors highlight a sublobe bias (see below). However, the independent empirical and computational approaches offer mutual support for localizing the binding domain to the C lobe, generating a model of sufficient accuracy to direct a further validation through mutational analysis.

A knowledge-based hot spot prediction algorithm was applied to the heterodimer models (37). For the *Ap*H49 TbpB-pTf dimer, residues Glu^{508} and Arg^{509} on pTf were identified as key contributors to binding energy, based on both shape complementarity and chemical features of the contact, in a wider contact region that is essentially equivalent to the 5 Å projection (Fig. 4 and supplemental Fig. 3). These pTf hot spots are mirrored by two amino acid hot spots on *Ap*H49 TbpB (Tyr^{162} and Phe^{171}). These two pTf residues demonstrate the strongest shape complementarity in the other two receptor-pTf complexes as well, although they fall just below the threshold for hotspots in the KFC model (37). For all three complexes, the remaining interfacial residues on pTf define a relatively homogeneous contact surface with respect to shape and atomic interactions. This computational characterization does not suggest the insignificance of the remaining interfacial residues, rather that the protein-protein interaction is not dominated by hot spots insofar as the computational method can identify them from a docked model.

Mutational Analysis of Binding Site—Several single amino acid mutations to pTf were then generated to test the proposed binding sites and to determine the significance of the predicted hot spot and other residues at the interface. The mutations selected for quantitative analysis were based upon a scan of eight residues within the interface, using a simple affinity capture method involving *Ap*H49 TbpB (supplemental Fig. 4). Only three mutations exhibited significant reductions in receptor binding via this method: D360A (C1 lobe, helix α1), S625K (C1 lobe, loop 23), and R509A (C2 lobe, loop 15). Designations of secondary structure follow the nomenclature of Hall *et al.* (38), and sublobe designations follow Hirose (40). Arg^{509} represents the putative hot spot, whereas Asp^{360} and Ser^{625} are

Downloaded from http://www.jbc.org/ at UNIVERSITY OF CALGARY on August 17, 2017

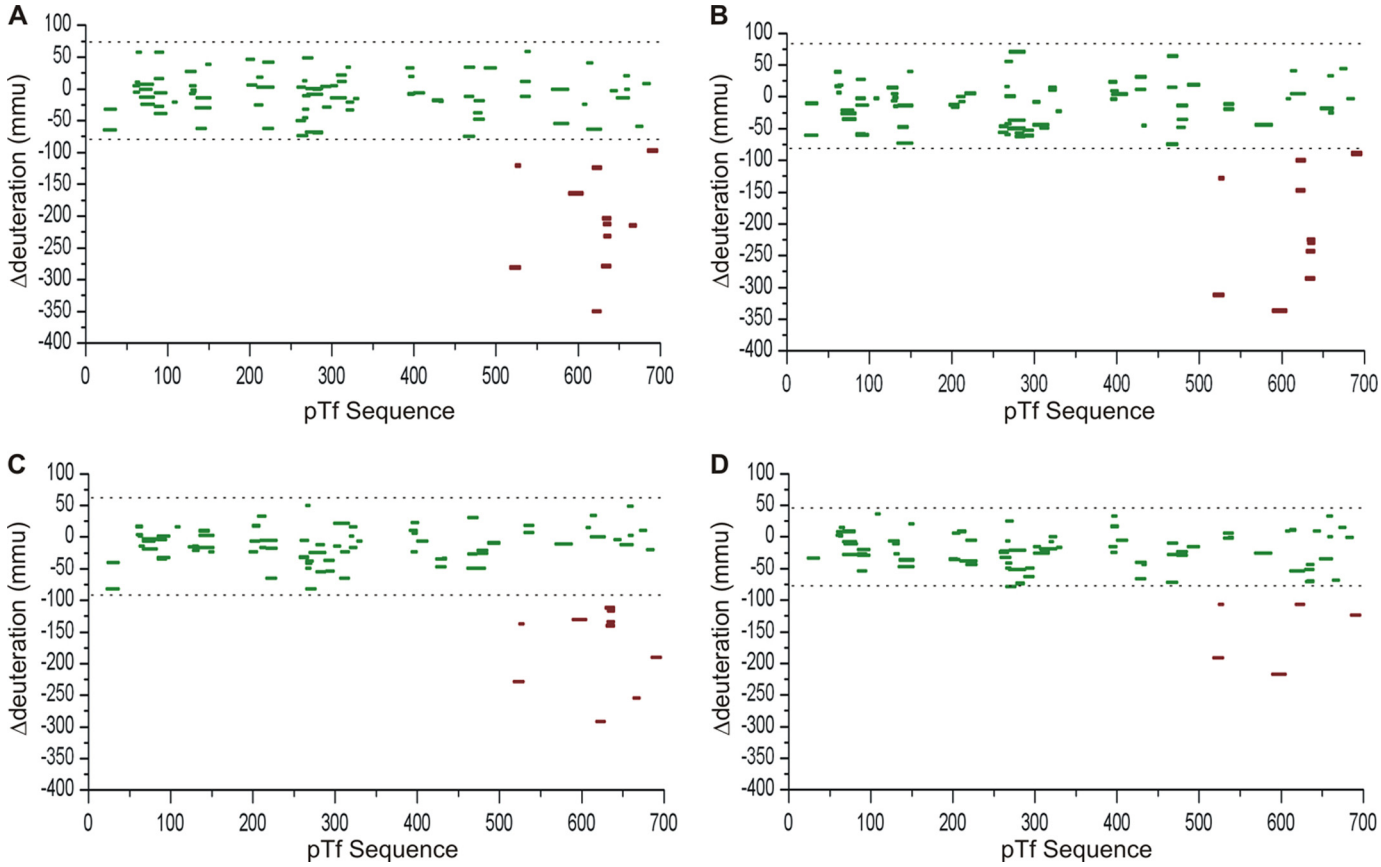

FIGURE 2. **Mass shift values for pTf-TbpB interactions.** Plots summarize the mass shifts induced by interaction of holo-pTf with *Ap*H49 TbpB (*A*), *Ap*H87 TbpB (*B*), *As*H57 TbpB (*C*), and *Ap*H89 TbpB (*D*). Significant alterations in peptide mass are represented as *red bars*, and insignificant shifts are in *green* using criteria described by Bennett *et al.* (33). *Dashed lines* mark the 95% confidence interval for the null hypothesis. The positioning of the *bars* indicates the location of the pepsin-generated peptides in the pTf sequence. All results from quadruplicate analyses.

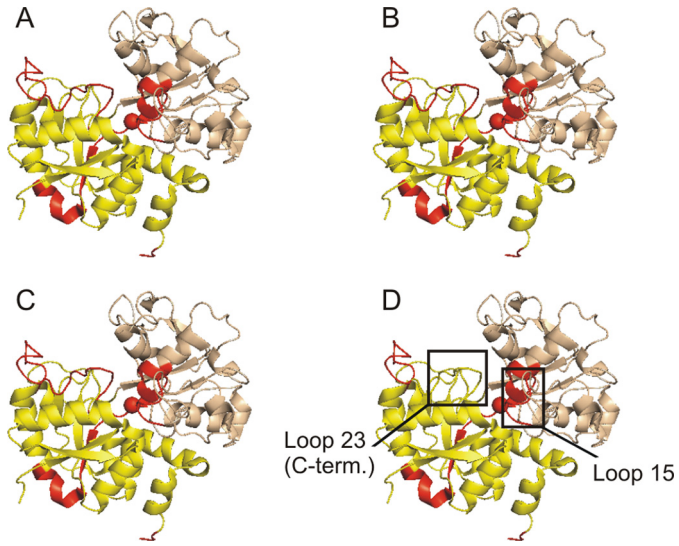

FIGURE 3. **Superposition of the receptor-induced mass shifts on pTf structure.** The figure maps the significant changes induced by *Ap*H49 TbpB (*A*), *Ap*H87 TbpB (*B*), *As*H57 TbpB (*C*), and *Ap*H89 TbpB (*D*). Changes are mapped in *red*, and as they cluster in the C lobe exclusively, only this region of pTf is shown. *Boxed* region in *D* represents the C terminus of loop 23, not protected from exchange in the interaction with *Ap*H89 TbpB. The orientation of pTf used in Fig. 1 is preserved.

oriented toward the receptor at the opposite end of the interface and on the opposing subdomain of the pTf C lobe (Fig. 4 and supplemental Fig. 3).

Binding studies using surface plasmon resonance (BiacoreX) generated kinetics data for wild-type pTf and each of the three mutant pTf proteins to each of the four receptor variants (Table 1 and supplemental Fig. 5). Wild-type pTf bound all four receptors with high affinity, generating K_d values consistent with previous measurements using isothermal calorimetry (*i.e.* 55 nM) (5). The data were conservatively fit using a 1:1 single-step binding model, but permitting heterogeneity. Direct immobilization can lead to a degree of variability in orienting the bound protein with respect to its cognate receptor, so this was considered the most appropriate model. A two-step model also provided a superior fit; however, this was ruled out after noting that variable contact time with the receptor did not significantly alter the kinetics of dissociation. The data arising from the major component in the heterogeneous fit is presented in Table 1 as the most reliable means of comparing the effect of mutations on binding. We used heterogeneous modeling for all mutated pTfs as well because these were immobilized in the same fashion as wild-type pTf.

These binding data show that the interaction is substantially weakened through a single mutation in the C2 sublobe. $\Delta\Delta G$ values range between 1.8 and 3.5 kcal/mol for the R509A mutation in loop 15, consistent with a hot spot. Mutations in the C1 sublobe had variable effects. A mutation in helix 1 (D360A) is strongly disrupting for variants *Ap*H49 and *Ap*H87 but does little to weaken binding for *As*H57 and *Ap*H89. A different

Downloaded from http://www.jbc.org/ at UNIVERSITY OF CALGARY on August 17, 2017

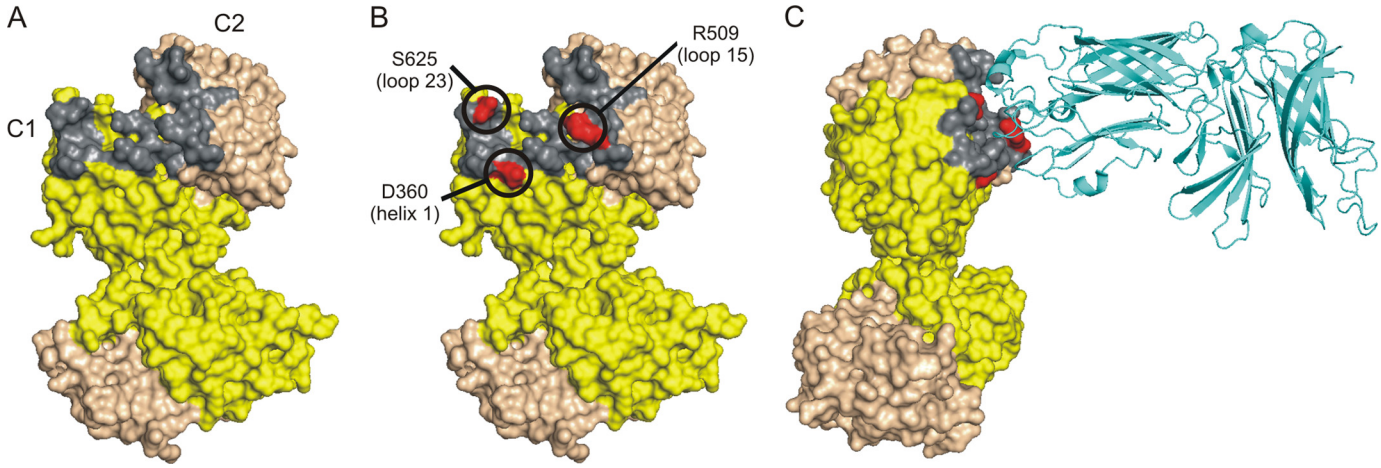

FIGURE 4. **Mapping of the proposed receptor interface on pTf.** *A*, surface representation of pTf, *oriented* and *color-coded* as in Fig. 1, with a projection of the *Ap*H49 TbpB interface highlighted in *gray*, based on a calculation of pTf residues within 5 Å of the receptor. Sublobes are labeled as C2 and C1. *B*, selection of residues within the proposed receptor binding site for mutational analysis, representing each sublobe. *C*, orientation of *Ap*H49 TbpB relative to pTf, arising from a Rosetta-docking exercise guided by confirmatory mutations in TbpB (31). Pose is +90° relative to *A* and *B*.

TABLE 1
Kinetics and thermodynamics of binding of pTf mutants to TbpB variants

Protein[a]	k_{on}	k_{off}	K_d	$\Delta\Delta G$
	$M^{-1}s^{-1}$	s^{-1}	nM	kcal/mol
Wild type				
*Ap*H49	1.75×10^5	7.7×10^{-3}	44 ± 1	
*Ap*H87	2.12×10^5	1.28×10^{-2}	60 ± 2	
*As*H57	2.52×10^5	3.06×10^{-2}	120 ± 4	
*Ap*H89	1.67×10^5	1.68×10^{-2}	100 ± 4	
C1 lobe (D360A)				
*Ap*H49	1.71×10^4	1.89×10^{-1}	11,000 ± 2,000	3.2
*Ap*H87	1.83×10^4	4.12×10^{-2}	2,200 ± 300	2.1
*As*H57	1.44×10^5	5.34×10^{-2}	370 ± 19	0.6
*Ap*H89	1.97×10^5	4.37×10^{-2}	222 ± 4	0.5
C1 lobe (S625K)				
*Ap*H49	5.46×10^5	1.87×10^{-1}	343 ± 6	1.2
*Ap*H87	2.02×10^5	8.28×10^{-2}	410 ± 8	1.1
*As*H57	5.82×10^4	9.22×10^{-2}	1,600 ± 100	1.5
*Ap*H89	4.69×10^5	1.29×10^{-1}	275 ± 8	0.6
C2 lobe (R509A)				
*Ap*H49	2.33×10^5	2.81×10^{-1}	1,200 ± 100	1.9
*Ap*H87	1.05×10^4	2.32×10^{-2}	2,200 ± 200	2.1
*As*H57	3.40×10^2	9.03×10^{-4}	2,600 ± 100	1.8
*Ap*H89	4.26×10^3	1.78×10^{-1}	41,000 ± 3,000	3.5

[a] The rate and dissociation constants were determined from sensorgrams involving the immobilization of pTf (wild type and mutants) and the infusion of free TbpB variants. Data were fit to a heterogeneous ligand binding model and report only the major component of binding. $\Delta\Delta G$ values were determined as $-RT\ln(K_{d,wt}/K_{d,mut})$.

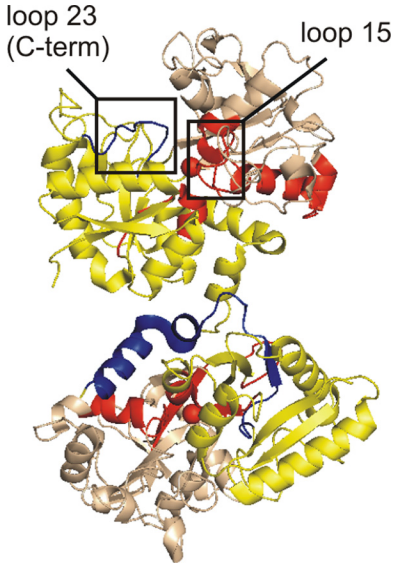

FIGURE 5. **Superposition of the iron-induced mass shifts on pTf.** Upon iron coordination, regions demonstrating increased protection are colored *red*, and those showing a decrease in protection are colored *blue*. The framed regions highlight changes that are unique to the C lobe, where the C terminus of loop 23 shows deprotection, and loop 15 shows protection. Both regions were identified as elements of the TbpB binding interface (see Figs. 2 and 3).

region of the C1 lobe may compensate for these two, with an obvious candidate being loop 23 (Fig. 4). However, a mutation in the C terminus of this loop (S625K) does not strongly affect binding for any of the four receptor variants we studied, but particularly for *Ap*H89. Overall, these mutational data highlight a central role for the C2 sublobe in the interface, where Arg^{509} in particular may be classified as a hot spot. The data also suggest that the C1 sublobe plays a minor role in binding but might contribute to high affinity interactions.

Stability Analysis of Bound versus Free pTf—Bridging two sublobes suggests a mechanism by which iron loading may influence the preference of TbpB for holo-pTf. To determine whether an iron-dependent conformational change in pTf is required for receptor binding, we tested the effect of iron loading on pTf stability. Mass shift analysis using H/D exchange was used to compare holo- and apo-pTf. Peptides with significantly altered mass induced by iron coordination were identified using the same criteria as in the receptor study (see summary in supplemental Fig. 6). As expected, a large number of overlapping peptide sequences show a decreased mass shift upon iron coordination, in both the N and C lobes. When mapped to the holo-pTf crystal structure (Fig. 5), these peptides localize specifically to the known iron coordination sites and an element of the C2 lobe (peptide 517–529, loop 15). However, iron unexpectedly induced an instability in two locations, shown as increased mass shifts upon iron coordination. One set of peptides localizes to the hinge region between the N and C lobes, suggesting that iron coordination induces greater flexibility between lobes. The other set is found in the C1 lobe (peptides 629 – 639, the C terminus of loop 23). In other words, iron coor-

Downloaded from http://www.jbc.org/ at UNIVERSITY OF CALGARY on August 17, 2017

dination stabilizes one region critical for receptor binding (loop 15) but destabilizes a second region shown to be part of the interface (loop 23). Both of these regions can be stabilized upon binding, although loop 23 is the region where the variability among receptors was noted. The corresponding sequences in the N lobe remain unchanged upon iron binding (Fig. 5).

Because the regions involved in iron coordination did not display changes in mass upon receptor binding, this suggests iron retention. To verify this, we performed a SUPREX analysis of the complex in the presence of FbpA, following established methods (13). Holo-FbpA is known to be substantially more stable than apo-FbpA, requiring higher concentrations of denaturant to induce unfolding (13). Thus, increased stabilization of FbpA in the presence the TbpB-pTf complex would indicate the capture of free iron released by the complex. SUPREX analysis using 0–4 M Gdn-HCl did not show any indication of iron capture by apo-FbpA when incubated with the *Ap*H49 TbpB-pTf complex (supplemental Fig. 7*A*). To confirm this finding, FbpA was isolated from solution (in the presence and absence of complex) and analyzed by spectrophotometry (supplemental Fig. 7*B*). No absorption at 480 nm was observed as a result of co-incubation with the complex. Together, these results show that iron is retained in the TbpB-pTf complex.

DISCUSSION

Characterizing the Interaction—Our analysis of the TbpB-pTf complex shows that an interaction with the C lobe of Tf is conserved, despite a considerable degree of sequence dissimilarity among the four receptor variants studied (31). The interaction can involve both subregions of the C lobe. Residue Arg^{509} on C2 is a hot spot for all receptor interactions, as is Asp^{360} on C1 for the two highest affinity receptors (*Ap*H49 and *Ap*H87) (37). The computational approach only highlights Arg^{509}, but this could be expected as the calculations are based on modeled structure. Nevertheless, identifying one of these sites through computation suggests a reasonably accurate mapping of the interfacial residues on Tf, if not the actual high resolution conformation. This level of accuracy awaits x-ray diffraction data from the crystallized complexes. The mass shift data, however, support the conclusion that both sublobes are involved in the interaction with variants *Ap*H49 and *Ap*H87 (Fig. 3 and supplemental Fig. 2).

For TbpB variant *Ap*H89, the mutational and mass shift data together suggest an interaction favoring the C2 sublobe on pTf. Based on the surface plasmon resonance measurements, Arg^{509} contributes strongly to the interaction, but the mutated C1 residues do not. It may be that untested residues on the C1 sublobe contribute more to binding free energy, but a minor role for the C1 sublobe is supported by weak or absent mass shifts in the H/D analysis (Fig. 3 and supplemental Fig. 2). Unfortunately, a structure of this TbpB variant is not yet available, so at this stage we cannot determine the extent to which the interface departs from the three modeled in this study.

With respect to C1 sublobe involvement, variant *As*H57 is quite similar to *Ap*H89. Its interaction is hardly altered by the D360A mutation in helix 1 (Table 1), and the C terminus of loop 23 does not become protected nearly as well as in the two highest affinity receptors (see supplemental Fig. 2). It is not surprising that the loop may not have a critical role in receptor binding. It is strongly destabilized upon iron binding (Fig. 5), suggesting an entropic penalty associated with engaging this region.

This conclusion is consistent with the structural classification of the receptors in the companion study (31). At the interface with pTf, *Ap*H49 and *Ap*H87 receptors are similar in the structure and orientation of their cap region. In both cases, critical binding residues interact with loop 23. *As*H57 is structurally divergent in its cap region, presenting a much different interface. Although it appears to interact with the C-terminal element of loop 23, there are few obvious contacts in the docked model. The structure for *Ap*H89 is not available, but we tentatively classify it with *As*H57 based on limited or nonexistent contact with the C1 sublobe. Taken as a whole, a high affinity interaction with pTf requires binding to both sublobes, but C1 may contribute to a minor degree, likely because of the large iron-induced destabilization of loop 23 in this region.

The unique conformational response of the C lobe to iron loading is a surprising finding, given the strong structural similarity between the C and N lobes, but this seems to support why TbpB is selective for the C lobe. Aligning the two domains shows that the corresponding region on the N lobe actually orients the regions of the proposed interface in a distinct fashion as well (supplemental Fig. 8). Together, the binding region of the C lobe is therefore structurally and conformationally distinct from the N lobe.

Mechanistic and Functional Significance—In contrast to mammalian Tf receptors on host cells, which function through receptor-mediated endocytosis and rely on of the acidification of the endosome to facilitate iron removal, bacterial receptors are responsible for extracting iron from Tf at the cell surface and transporting iron across the outer membrane. TbpB is a critical component in the recognition of the iron-loaded form of Tf (20, 21) and is consistent across all variants studied in C lobe targeting (11, 31).

However, its role in iron release is not fully understood. Reporting on the interaction between human Tf and TbpB from human pathogens, Nemish *et al.* did not detect an independent role in iron release (41). It was suggested recently that both TbpA and TbpB can facilitate the transfer of iron from human Tf to FbpA in membranes isolated from *Neisseria gonorrhoeae* (13). Our SUPREX and spectrophotometric data, based on sensitive measurements of iron scavenging using FbpA, show that the isolated TbpB-pTf complex does not appear to influence iron release, supporting Nemish *et al.*, but a function involving the membrane environment cannot be ruled out.

The ability of TbpB to identify the iron-loaded form of the C lobe may be advantageous under the conditions of the mucosal surface that these bacteria inhabit. Although there is no direct information on the states of Tf iron loading at the mucosal surfaces, the monoferric C lobe form was shown to be dominant in serum samples from different sites (42). The pH of the mucosal surface is slightly acidic, and because the monoferric C lobe is relatively more stable than the N lobe under conditions of lower pH, it is possible that the dominance of monoferric C lobe is further enhanced at the mucosal surface.

Downloaded from http://www.jbc.org/ at UNIVERSITY OF CALGARY on August 17, 2017

The results from this study therefore favor a model whereby TbpB functions to capture iron-loaded Tf efficiently, regardless of the iron status of the host, for presentation to TbpA. This would generate efficient uptake because TbpA does not discriminate between apo- or holo-states (22, 23). Further insights will require experiments involving TbpA and additional elements possibly involved in releasing iron from a TbpB-bound Tf state.

Our results also highlight a consistent binding motif on pTf, which seems to hold for human Tf and the corresponding human pathogens (11). Although our companion study points to a degree of variability within the receptor binding site (31), the conserved nature of the Tf-binding motif does suggest the existence of a reciprocally conserved epitope within the TbpB receptor. The current study therefore supports the pursuit of a broad spectrum vaccine targeting TbpB, particularly when coupled with the general observation that TbpB is present in all clinical isolates.

REFERENCES

1. West, S. E., and Sparling, P. F. (1985) *Infect. Immun.* **47,** 388–394
2. Schryvers, A. B., and Morris, L. J. (1988) *Mol. Microbiol.* **2,** 281–288
3. Gray-Owen, S. D., and Schryvers, A. B. (1995) *Infect. Immun.* **63,** 3809–3815
4. Schryvers, A. B., and Stojiljkovic, I. (1999) *Mol. Microbiol.* **32,** 1117–1123
5. Moraes, T. F., Yu, R. H., Strynadka, N. C., and Schryvers, A. B. (2009) *Mol. Cell* **35,** 523–533
6. Mickelsen, P. A., and Sparling, P. F. (1981) *Infect. Immun.* **33,** 555–564
7. Mickelsen, P. A., Blackman, E., and Sparling, P. F. (1982) *Infect. Immun.* **35,** 915–920
8. Lee, B. C., and Schryvers, A. B. (1988) *Mol. Microbiol.* **2,** 827–829
9. Dyer, D. W., West, E. P., and Sparling, P. F. (1987) *Infect. Immun.* **55,** 2171–2175
10. Jacques, M. (2004) *Can. J. Vet. Res.* **68,** 81–85
11. Ling, J. M., Shima, C. H., Schriemer, D. C., and Schryvers, A. B. (2010) *Mol. Microbiol.* **77,** 1301–1314
12. Cornelissen, C. N., Kelley, M., Hobbs, M. M., Anderson, J. E., Cannon, J. G., Cohen, M. S., and Sparling, P. F. (1998) *Mol. Microbiol.* **27,** 611–616
13. Parker Siburt, C. J., Roulhac, P. L., Weaver, K. D., Noto, J. M., Mietzner, T. A., Cornelissen, C. N., Fitzgerald, M. C., and Crumbliss, A. L. (2009) *Metallomics* **1,** 249–255
14. Schryvers, A. B., and Gonzalez, G. C. (1990) *Can. J. Microbiol.* **36,** 145–147
15. Criado, M. T., Pintor, M., and Ferreirós, C. M. (1993) *Res. Microbiol.* **144,** 77–82
16. Bobst, C. E., Zhang, M., and Kaltashov, I. A. (2009) *J. Mol. Biol.* **388,** 954–967
17. Halbrooks, P. J., He, Q. Y., Briggs, S. K., Everse, S. J., Smith, V. C., MacGillivray, R. T., and Mason, A. B. (2003) *Biochemistry* **42,** 3701–3707
18. Bailey, S., Evans, R. W., Garratt, R. C., Gorinsky, B., Hasnain, S., Horsburgh, C., Jhoti, H., Lindley, P. F., Mydin, A., and Sarra, R. (1988) *Biochemistry* **27,** 5804–5812
19. Giannetti, A. M., Halbrooks, P. J., Mason, A. B., Vogt, T. M., Enns, C. A., and Björkman, P. J. (2005) *Structure* **13,** 1613–1623
20. Boulton, I. C., Gorringe, A. R., Allison, N., Robinson, A., Gorinsky, B., Joannou, C. L., and Evans, R. W. (1998) *Biochem. J.* **334,** 269–273
21. Renauld-Mongenie, G., Latour, M., Poncet, D., Naville, S., and Quentin-Millet, M. J. (1998) *FEMS Micro. Lett.* **169,** 171–177
22. Retzer, M. D., Yu, R. H., and Schryvers, A. B. (1999) *Mol. Microbiol.* **32,** 111–121
23. Yu, R. H., and Schryvers, A. B. (1993) *Microbial Pathogenesis* **15,** 433–445
24. Krell, T., Renauld-Mongénie, G., Nicolaï, M. C., Fraysse, S., Chevalier, M., Bérard, Y., Oakhill, J., Evans, R. W., Gorringe, A., and Lissolo, L. (2003) *J. Biol. Chem.* **278,** 14712–14722
25. DeRocco, A. J., and Cornelissen, C. N. (2007) *Infect. Immun.* **75,** 3220–3232
26. Baltes, N., Hennig-Pauka, I., and Gerlach, G. F. (2002) *FEMS Micro. Lett.* **209,** 283–287
27. Perkins-Balding, D., Ratliff-Griffin, M., and Stojiljkovic, I. (2004) *Micro. Mol. Biol. Rev.* **68,** 154–171
28. Renauld-Mongénie, G., Poncet, D., Mignon, M., Fraysse, S., Chabanel, C., Danve, B., Krell, T., and Quentin-Millet, M. J. (2004) *Infect. Immun.* **72,** 3461–3470
29. Vonder Haar, R. A., Legrain, M., Kolbe, H. V., and Jacobs, E. (1994) *J. Bacteriol.* **176,** 6207–6213
30. Alcantara, J., Yu, R. H., and Schryvers, A. B. (1993) *Mol. Microbiol.* **8,** 1135–1143
31. Calmettes, C., Yu, R. H., Silva, L. P., Curran, D., Schriemer, D. C., Schryvers, A. B., and Moraes, T. F. (2011) *J. Biol. Chem.* **286,** 12683–12692
32. Mandell, J. G., Falick, A. M., and Komives, E. A. (1998) *Proc. Natl. Acad. Sci. U.S.A.* **95,** 14705–14710
33. Bennett, M. J., Barakat, K., Huzil, J. T., Tuszynski, J., and Schriemer, D. C. (2010) *Chem. Biol.* **17,** 725–734
34. Weiner, M. P., Costa, G. L., Schoettlin, W., Cline, J., Mathur, E., and Bauer, J. C. (1994) *Gene* **151,** 119–123
35. Shouldice, S. R., Dougan, D. R., Skene, R. J., Tari, L. W., McRee, D. E., Yu, R. H., and Schryvers, A. B. (2003) *J. Biol. Chem.* **278,** 11513–11519
36. Slysz, G. W., Percy, A. J., and Schriemer, D. C. (2008) *Anal. Chem.* **80,** 7004–7011
37. Darnell, S. J., Page, D., and Mitchell, J. C. (2007) *Proteins* **68,** 813–823
38. Hall, D. R., Hadden, J. M, Leonard, G. A., Bailey, S., Neu, M., Winn, M., and Lindley, P. F. (2002) *Acta Crystallogr. D Biol. Crystallogr.* **58,** 70–80
39. Shen, Z. M., Yang, J. T., Feng, Y. M., and Wu, C. S. (1992) *Protein Sci.* **1,** 1477–1484
40. Hirose, M. (2000) *Biosci. Biotechnol. Biochem.* **64,** 1328–1336
41. Nemish, U., Yu, R. H., Tari, L. W., Krewulak, K., and Schryvers, A. B. (2003) *Biochem. Cell Biol.* **81,** 275–283
42. Vogel, W., Herold, M., Margreiter, R., and Bomford, A. (1989) *Klinische Wochenschrift* **67,** 538–542

Downloaded from http://www.jbc.org/ at UNIVERSITY OF CALGARY on August 17, 2017

Conserved Interaction between Transferrin and Transferrin-binding Proteins from Porcine Pathogens

Leslie P. Silva, Ronghua Yu, Charles Calmettes, Xue Yang, Trevor F. Moraes, Anthony B. Schryvers and David C. Schriemer

J. Biol. Chem. 2011, 286:21353-21360.
doi: 10.1074/jbc.M111.226449 originally published online April 12, 2011

Access the most updated version of this article at doi: 10.1074/jbc.M111.226449

Alerts:
- When this article is cited
- When a correction for this article is posted

Click here to choose from all of JBC's e-mail alerts

Supplemental material:
http://www.jbc.org/content/suppl/2011/04/20/M111.226449.DC1

This article cites 42 references, 14 of which can be accessed free at
http://www.jbc.org/content/286/24/21353.full.html#ref-list-1

Downloaded from http://www.jbc.org/ at UNIVERSITY OF CALGARY on August 17, 2017